EFDA–JET–PR(11)55

H. Weisen, Y. Camenen, A. Salmi, T.W. Versloot, P.C. deVries, M. Maslov,
T. Tala, M. Beurskens, C. Giroud and JET EFDA contributors

Ubiquity of Non-diffusive Momentum Transport in JET H-modes

Ubiquity of Non-diffusive Momentum Transport in JET H-modes

H. Weisen[1], Y. Camenen[2], A. Salmi[3], T.W. Versloot[4], P.C. deVries[4], M. Maslov[5], T. Tala[6], M. Beurskens[5], C. Giroud[5] and JET EFDA contributors*

JET-EFDA, Culham Science Centre, OX14 3DB, Abingdon, UK

[1]Centre de Recherches en Physique des Plasmas, Association EURATOM - Confédération Suisse, EPFL, 1015 Lausanne, Switzerland
[2]PIIM UMR 7345, CNRS/Aix-Marseille Univ., France
[3]Association EURATOM-Tekes, Aalto University, Finland,
[4]FOM Institute Rijnhuizen, Association EURATOM-FOM, The Netherlands
[5]EURATOM-CCFE Fusion Association, Culham Science Centre, OX14 3DB, Abingdon, OXON, UK
[6]Association EURATOM-Tekes, VTT, Finland
** See annex of F. Romanelli et al, "Overview of JET Results", (23rd IAEA Fusion Energy Conference, Daejon, Republic of Korea (2010)).*

Preprint of Paper to be submitted for publication in
Nuclear Fusion

ABSTRACT.
A broad survey of the experimental database of neutral beam heated baseline H-modes and hybrid scenarios in the JET tokamak has established the ubiquity of non-diffusive momentum transport mechanisms in rotating plasmas. As a result of their presence, the normalised angular frequency gradient $R\,\nabla\omega/\omega$ is higher than expected from momentum diffusion alone, by about unity in the core (r/a~0.3), rising to near 5 close to the edge, where its contribution to the total gradient is comparable to the gradient associated with the diffusive flux. The magnitude and parameter dependencies of the non-diffusive contribution to the gradient are consistent with a theoretically expected pinch, which has its origin in the vertical particle drift resulting from the Coriolis force. Linear gyrokinetic calculations of the pinch number RV/χ_ϕ and the Prandtl number χ_ϕ/χ_i, are in good agreement with the experimental observations, with similar dependencies on R/L_n, q and $\varepsilon = r/R$. A contribution due to residual stresses may also be present, but could not be identified with certainty.

1.INTRODUCTION

In recent years, substantial experimental evidence for momentum transport processes that cannot be attributed to diffusion alone has been reported from several tokamaks [1-20], including JET [2,3]. Non-diffusive momentum transport is theoretically expected to be driven by drift wave turbulence in the form of a pinch and/or residual stresses [21,22]. The pinch is now theoretically rather well understood [23-36]. In the frame of reference rotating with the plasma, the pinch arises from the Coriolis force which causes a vertical drift proportional to the parallel velocity and to the frame rotation frequency. This drift leads to a momentum flux proportional to the angular rotation frequency (i.e. a pinch) by coupling turbulent density and parallel velocity perturbations [23]. An equivalent description in the laboratory frame of reference is given in ref. [24]. The residual stress part involves a variety of mechanisms, all leading to momentum flux contributions of comparable magnitude and potentially opposite signs. The present study focuses on the pinch, expected to be the largest in JET strongly rotating plasmas, and the reader is referred to refs [21] and [22] and the references therein for an extensive discussion on the theoretical advances on residual stress.

In the JET device [37], evidence for an inward momentum pinch originated from Neutral Beam Injection (NBI) modulation experiments obtained largely in fairly quiescent, low power H-modes and a few L-modes [2,3]. These findings motivated a broad based database survey destined to establish to which extent the pinch identified in those experiments was ubiquitous and in particular, if it was present in higher power, higher performance baseline H-modes and hybrid scenarios. The latter provide and improvement over baseline confinement resulting from a reduction of magnetic shear over much of the plasma profile [38]. A supplementary goal was to compare the experimental data over the entire JET NBI heated H-mode and hybrid scenario operating domains to theoretical predictions, in order to validate or invalidate, as may be, the expectation that these strongly rotating plasmas (with Mach numbers $u = v_\phi/v_i$ up to 0.35) are subject to non-diffusive transport arising mainly from the Coriolis pinch [23-36]. The database constituted for this purpose

covers the entire JET operating domain in baseline H-mode and hybrid scenarios and contains several hundred steady-state profiles of the relevant plasma parameters. Together baseline H-mode and hybrid scenarios constitute the mainstay of the JET operating domain over recent years and provide two of the main scenarios foreseen for the ITER project [39].

2. STATISTICAL METHOD

The method is to test whether the normalised gradients follow a dimensionless normalised diffusion-convection equation with a tractable (i.e. limited) number of dependencies, e.g dependencies consistent with the theoretically predicted Coriolis pinch [23-36]. To this effect, we write the local steady state momentum transport equation as

$$t = -\chi_\phi\, l\nabla\omega/\omega + (\Gamma_N/n_i + V)\, l + \tau_{rs} \tag{1}$$

Here $t = T/(dV_{FS}/dr)$ is the local torque surface density (N/m) from NBI, with $T(r)$ the volume integrated torque density, $V_{FS}(r)$ the volume of the flux surface and r the average midplane minor radius. $l = m_i n_i R^2 \omega$ is the angular momentum density, m_i the average ion mass, n_i the ion density, R the average major radius of the flux surface under consideration, ω the toroidal angular velocity, Γ_N is the particle flux associated with the particle source provided by neutral beam heating, χ_ϕ is the radial momentum diffusivity, V is the momentum pinch velocity, and τ_{rs} refers to residual stress contributions. In addition to the torque associated with NBI, torques resulting from fast ion losses and charge exchange losses may have to be considered, especially near the plasma boundary. A previous study has shown that in the bulk plasma, the particle source associated with the penetration of edge neutrals can be neglected [40]. In the conditions of JET NBI H-modes and hybrid scenarios, the pinch term is expected to dominate over the residual stresses [21]. Eq.(1) is rearranged, written in dimensionless form and normalized as:

$$R\frac{\nabla\omega}{\omega} = -\frac{\chi_i}{\chi_\phi}\left\{\frac{Rt}{\chi_i l} - \frac{R\Gamma_N}{\chi_i n_i}\right\} + \frac{RV}{\chi_\phi} + \frac{R\tau_{rs}}{\chi_\phi l} \tag{2}$$

In eq.(2), $\chi_i = Q_i/(n_i\, T_i)$ is the ion heat diffusivity, which is determined from the local power balance as $Q_i = Q_{iNB} + Q_{ei}$ [W/m^2], where Q_{iNB} is the ion heat flux provided by the neutral beams and Q_{ei} is the electron-ion equipartition flux. About one third of the samples included a modest fraction of hydrogen minority Ion Cyclotron Resonance Heating (ICRH), which mostly heats the electrons. Any ion heating from ICRH was neglected in this study. The normalized angular velocity gradient in eq.(2) was obtained from CXRS measurements, while the term between brackets, the normalized net dimensionless torque $t_i^* - \Gamma_N^*$, was obtained from a combination of measurements and calculations. An alternative form for eq.(2), suitable for dataset containing low values of ω (i.e. large errors on $R\nabla\omega/\omega$) is obtained by multiplying eq.(2) by $u = Rw/v_i = Rw/(2T_i/m_i)^{1/2}$, the Mach number. In this form, the residual stress is represented by the regression constant. In JET NBI

H-modes and hybrid scenarios, near zero rotation is only obtained near the edge in the presence of strong toroidal ripple [41].

For a sufficiently well conditioned database, the form of eq.(2) lends itself in principle to determining the Prandtl number χ_ϕ/χ_i and the pinch number RV/χ_ϕ, as well as a possible residual stress contribution, by means of regression techniques. The residual stress term may be written as

$$\frac{R\tau_{rs}}{\chi_\phi l} = \frac{\tau_{rs}}{m_i n_i v_i \chi_\phi} \frac{1}{u} \tag{3}$$

suggesting that the different scaling with u may allow distinguishing it from the pinch. Unfortunately, so far no reliable separation of the two non-diffusive terms has been obtained on the basis of the different scaling with u only, whether using eq.(2) as such or multiplied by u. In this paper we therefore lump the two terms together in eq.(2) in a single dimensionless number characterizing the non-diffusive processes, $RV/\chi_\phi + \tau_{rs}*/u$, where $\tau_{rs}* = \tau_{rs}/(m_i n_i v_i \chi_\phi)$ is a dimensionless residual stress number and leave a tentative discussion of their respective importance to section 8.

3. DATA SET DESCRIPTION

The database used evolved from the JETPEAK profile database used for density peaking studies [42,43], by including the required variables and data from the last experimental campaigns in the carbon wall configuration (up to the year 2009), as well as samples from a previous rotation database [44]. It contains several hundred steady-state profiles measured using standard diagnostics such as CXRS [45] of intrinsic carbon impurities for angular velocity and ion temperature and Thomson scattering for electron density and temperature. Whenever possible, the electron temperature and density were taken using the high resolution Thomson scattering diagnostic [46], otherwise using the JET LIDAR [47]. Most of the H-modes achieved global confinement improvement factors H98 with respect to the IPB98(y,2) global multi-machine scaling [48] in the range 0.6-1, while recent hybrid regimes had H98 factors up to 1.45, an improvement frequently attributed to a more favourable magnetic shear profile or a combination of low magnetic and high rotational shear [49]. As the more recent profile data appear to be of better quality, the data used here include only discharges with JET pulse numbers larger than 59000, produced in 2003 and later.

The particle flux term in eq.(2) is a small (~10%) correction to the gross torque from the NBI, as shown in figure 1 for a large number of samples taken at mid-radius. The ion heat flux Q_{iNB} from the neutral beams was evaluated using the beam deposition code PENCIL [50], which does not take into account ion orbit effects, i.e. no distinction is made between the instantaneous torque due to beam ion trapping and the collisional torque conferred to the plasma by passing ions. The code simply assumes that the neutral energy and momentum are deposited at the flux surface where the neutral is ionised. The different time scales are not of relevance here, since the dataset only comprises samples in steady state for at least one second, which is longer than the fast ion slowing down time. However the orbit effects lead to changes in the heat and momentum deposition profiles

with respect to those calculated using PENCIL. A small correction was therefore applied to Q_{iNB} and t obtained from PENCIL to bring these into line with more accurate calculations, effected for a small subset, using the ASCOT Monte Carlo orbit following code [51]. Because ASCOT calculations are laborious and cannot be performed for the whole dataset of interest, we have compared the PENCIL and ASCOT derived torque and ion heat flux profiles t [Nm/m^2] and Q_{iNB} [W/m^2] for a set of representative samples in order to obtain a zero order correction for t/Q_i, which enters the definition of the dimensionless torque, $t_i^* = Rt/(l\chi_i)=Rt/(l(Q_{iNB}+Q_{ei}))/(n_i\ T_i))$. The corrected torque profile t was calculated from the PENCIL profile as $t = t_{PENCIL}\ (<t_{ASCOT}/t_{PENCIL}>)$ and likewise for Q_{iNB}. Here < > represents an average over the 10 available profiles from ASCOT calculations. Not performing this correction has little influence on the statistical analysis for non-diffusive transport presented in this paper, but would lead to an overestimate of the Prandtl number by some 20%.

A small subset with a scan of toroidal ripple $\Delta B_T/B_T$ from the usual 0.08% to 1% outboard midplane LCFS was also included. For this set full ASCOT calculations were performed because the differences between ASCOT and PENCIL torque profiles are very substantial due the large ion losses in the periphery (r/a>3/4) in the presence of toroidal ripple [41]. As an accurate determination of the power balance is necessary for evaluating χ_i, we restricted the data to those where the equipartition flux Q_{ei}, which is subject to fairly large uncertainties, is smaller in magnitude than $0.35Q_i$. Despite this restriction, the data cover a wide range in dimensionless parameter space, as shown in table 1.

The gradients are evaluated in the equatorial plane as averages between the high and low field side, following a tensioned spline fit over the profile data. As the trapped particle fraction, $f_t\varepsilon^{1/2}$, is an important physics parameter for momentum transport [27], all profiles were mapped onto ε as the radial coordinate. We have not included positions closer to the LCFS than $\varepsilon = 0.255$ (r/a = 0.85) in order to avoid any hard to quantify contributions of ion loss and charge exchange torques to the momentum balance.

Linear gyrokinetic drift wave stability calculations for a large representative sample of the database, presented in section 7, show that they are all in the Ion Temperature Gradient (ITG) domain. The ordering parameter $O_{rs} = \rho_i^*(R/L_{Ti})^2/u$ is in the range 0.07–1 for 92% of the 944 samples in the database and below 0.5 for 62% of the samples, indicating, according to theory [21], that the pinch, rather than residual stresses, is the most important non-diffusive transport mechanism for the majority of the conditions in the database.

Nearly half of the samples the database include Ion Cyclotron Resonance Heating (ICRH), providing up to 40% of the total heating power, using the hydrogen minority resonance scheme, which produces fast hydrogen ions and therefore mainly provides collisional electron heating[53]. In a recent study, H-minority ICRH in plasmas heated only by ICRH was not observed to drive significant rotation in JET [54]. An older study in L-mode [55] reported on the observation of rotation in ICRH-only discharges, with frequencies *(< 6 krad/s*) typically one order of magnitude below those in our H-mode database *(<130 krad/s)*. Differences between co- and counter antenna

phasing, which may be an indication of momentum transfer by waves, were typically about *2 krad/s*, suggesting that intrinsic rotation, rather than ICRH driven rotation may dominate in many ICRH-only discharges. As a result, we are not concerned that an unaccounted for momentum source resulting from ICRH may significantly affect our analysis. Nonetheless, as a matter of precaution, we have limited the database to samples where ICRH represents less than 40% of the total input power.

4. SIMPLE REGRESSIONS

Figure 2 shows simple regressions (without a specific term for residual stresses) for three positions, $\varepsilon \approx 0.075$, $\varepsilon \approx 0.165$ and $\varepsilon \approx 0.255$. The symbols are resolved by the Mach number u. Except for the innermost position, the relationship between the net dimensionless torque t_i^*-Γ_N^* and R/L_ω does not depend on u. It also does not depend on confinement quality as measured by the confinement merit factor H98. The presence of a diffusive part scaling linearly with t_i^*-Γ_N^* is clearly visible at all three positions. At $\varepsilon \approx 0.165$ and $\varepsilon \approx 0.255$ a significant offset shows that a significant non-diffusive part is also present.

The regressions in fig.2 are part of a profile, shown in fig.3, constituted of 7 partly overlapping intervals, shown as horizontal bars, over which gradients were evaluated. The vertical bars indicate the 90% confidence intervals for the regressions. The last closed flux surface is typically at $\varepsilon = 0.3$. The figure shows that the non-diffusive component (fig.3a) increases markedly towards the plasma boundary, while the Prandtl number (fig.3b) is close to unity, without a significant radial dependence. Not applying the above mentioned orbit effect corrections, or excluding all shots with ICRH, does not lead to any significant changes in the non-diffusive terms evaluated from the regressions. The non-diffusive transport, together with the the substantial rotation pedestal (more than 30% of the core value in most cases) has the perhaps counter-intuitive effect of making the angular frequency profiles slightly broader (rather than more peaked) than the ion temperature profiles. The strong non-diffusive inward transport near the edge, acting on the pedestal rotation, has the effect of steepening the gradients near the edge more than further inside, where non-diffusive transport is weaker. This leads to angular rotation profiles peaking factors $\omega(0)/\langle\omega\rangle$ which on average are 10% lower than the peaking factors for the ion temperature, $T_i(0)/\langle T_i\rangle$, the brackets designating volume averages.

Figure 3 also shows the results from two much smaller and less well conditioned datasets (~20 samples per position). The first of these, shown as open blue circles, is assembled in steady state conditions from a set of experiments used to determine the momentum pinch using modulation techniques [2,3]. The much wider confidence intervals are not shown for clarity, but are in the range 1-2 for the non-diffusive part and 0.2-1 for the Prandtl number. No meaningful regressions were obtained for the innermost two positions. The regression results for the non-diffusive component are in good agreement with the modulations results, for which typical pinch numbers in the range 4 to 6 were obtained for $\varepsilon > 0.12$.

The second dataset, the results of which are shown by a red 'x' is from a series of discharges where the toroidal ripple at the low field side Last Closed Flux Surface (LCFS) was varied in the range 0.08 to 1% [56]. The ion losses caused by the ripple produce an edge torque in the counter-current direction, which for a ripple of 1%, is of similar magnitude as the NBI torque. For these discharges the torque, consisting of the torque deposited by NBI and the torque due to the loss of beam and thermal ions, was calculated using the ASCOT code [51]. The innermost 5 positions produce regressions consistent with the main dataset, while for the outermost two positions regressions were poor, with confidence intervals larger than the regression coefficients, due to the presence of a small number samples with very high values of R/L_ω (>1000) and hence large uncertainties. They remained poor even when the alternative form of eq.(2), multiplied by u, was used. It is possible that the assumption of no radial electrical field in these ASCOT calculations, as well as the neglect of thermal ion losses in the presence of toroidal ripple, leads to misestimates of the torque associated with ion losses near the plasma boundary.

5. JETTO MODELLING OF MOMENTUM TRANSPORT IN THE PRESENCE OF ENHANCED TOROIDAL RIPPLE

The above general observations are supported by simulations of specific discharges with and without additional toroidal field ripple, using the JETTO transport code [56]. The increase in ripple beyond the normal value (0.08%) at the outboard midplane LCFS is produced by a slight reduction in the current in every other toroidal field coil. Fig. 4a shows the momentum and torque density profiles from two otherwise similar H-mode discharges with H98~0.8, one of which had 1% toroidal ripple. The total torque injected by the neutral beams was approximately 15 Nm with a NBI power of 15.4MW and 17.2MW respectively, in order to compensate the loss power from the increased ripple induced orbit losses. The torque per unit area (Nm/m^2) was roughly similar up to $r/a\sim0.8$ with the counter torque from the TF ripple largest in the outer region (fig 4b). The ion orbit losses calculated using ASCOT cause the net torque density to drop to near zero in the ripple case, leading to a large reduction in toroidal momentum throughout the plasma.

The two discharges had fairly high electron densities ($\sim6.5\times10^{19}m^{-3}$), corresponding to 80% of the Greenwald limit, similar density profiles with $R/L_n\approx2$ at mid-radius, similar ion and electron temperature profiles with $T_i \approx T_e$, and similar heat diffusivities, with χ_i in the range $0.4\text{-}1.3m^2/s$ for the interval $0.2<r/a<0.85$, as determined using the transport code JETTO. The same JETTO calculations, using a diffusive-convective model for momentum transport, show that the differences in the momentum profiles in the two discharges can be explained solely by the differences in torque, if a single Prandtl number profile for both discharges and a single pinch number profile with RV/χ_ϕ rising from the core to the edge, are assumed. A wide range of profiles was tested. The best simulations were obtained assuming a Prandtl number near unity and slightly rising with minor radius, and a pinch number rising from around 2 in the core to 8 at the edge (fig.4.c). When no non-diffusive flux was assumed to be present, different Prandtl number profiles were required for both discharges.

The conclusions from modeling are consistent with the above database analysis for the Prandtl number and for the non-diffusive component, although in this case it appears to be somewhat larger than the average from the database.

6. MULTI-PARAMETER REGRESSIONS

Multiple parameter dependencies were investigated by testing and ranking hundreds of the parameter combinations. As a result of unavoidable correlations in the database, several fits of similar quality (in terms of root mean square differences between the fit and the experimental data) can be obtained with different parameter combinations. Combinations including t_i*-Γ_N*, R/L_n, q, s, ε, T_i/T_e and R/L_{Ti} or R/L_{Te} provide the best regressions. It should be noted that the coefficients for any parameter vary depending on the other parameters of the fit and are not necessarily indicative of the underlying physics dependencies, which may not only be different, but also may not be reducible to simple linear dependencies over the wide JET parameter space.

Tables 2a) and 2b) below provide an idea of the correlations in the database at two of the seven sampling positions, $\varepsilon = 0.165$ and $\varepsilon = 0.255$.

The tables show that t_i*-Γ_N* is only weakly correlated with the other variables, with the important exception of R/L_{Ti} , which it strongly correlates with. Those two variables should therefore not be used together in a regression. This correlation can be understood from the fact that the ion heating and momentum deposition profiles and the diffusive components of ion heat and momentum transport are strongly related. If t_i*-Γ_N* and R/L_{Ti} are used together in a regression, the diffusive part is largely 'absorbed' into the coefficient for R/L_{Ti}, leading to an erroneous value for the Prandtl number, which then is well above unity. We also note that the classical dimensionless parameters governing drift wave transport, ν_{eff}, β and ρ_i^*, are not or only very weakly correlated with R/L_ω, and with t_i*-Γ_N* and hence with any non-diffusive component inferred from the difference between those two. In particular, the correlation of R/L_ω with ρ_i* is insignificant. This is important, because ρ_i* is the single most important extrapolation parameter from current devices towards ITER.

Although many regressions with similar standard deviations are easily obtained by automatically regressing and ranking all possible parameter combinations, only those for which all the regression coefficients are statistically significant and statistically relevant are of interest. The regressions shown below are given with their fit coefficients (b), their uncertainty δb corresponding to a 90% confidence level, the statistical significance $b/\delta b$, labeled STS, and the statistical relevance labeled STR. The latter is defined, for each parameter i, as $b_i\sigma_i/\sigma_{target}$, where σ_i is the standard deviation of parameter i and σ_{target} is the standard deviation of the target variable, R/L_ω. The STR indicates which part of the variations of the target variable can be attributed to the variations of the regression variable. We shall typically restrict ourselves to regressions where all coefficients satisfy $STS \geq 1$ and $STR \geq 0.08$.

Figures 5a and 5b show the best regressions for the same two positions as in table 1. The data are resolved into classes of confinement merit factors H98, in order to show that H98 has no influence

on these dimensionless relationships. For $\varepsilon = 0.165$, only two parameters can be fitted such as to satisfy our significance criteria, while for $\varepsilon = 0.255$, where the non-diffusive components are strongest, up to 5 parameters can be fitted. The two regressions correspond to:

$$\text{At } \varepsilon = 0.165\text{: } R/L_\omega \; 1.1(t_i{}^*\text{-}\Gamma_N{}^*)\text{-}2.8T_i/T_e\text{+}5.3 \tag{4}$$

The standard deviation σ, the statistical significance STS and relevance STR, in the order of appearance of the variables in eq.(4), are

$$\sigma = 0.91,\ STS = [7.3,\ 2.1,\ 3.9] \text{ and } STR = [0.72,\ 0.2.\ 0].$$

$$\text{At } \varepsilon = 0.255\text{: } R/L_\omega \; 1.1(t_i{}^*\text{-}\Gamma_N{}^*)\text{+}0.47R/L_n\text{+}0.71q\text{+}0.22R/L_{Te}\text{ -}2.8T_i/T_e\text{+}2.9 \tag{5}$$

$$\text{with } \sigma = 1.74,\ STS = [6.1,\ 2.1,\ 1.3, 1.2, 1.8,\ 0.9],\ STR = [0.65,\ 0.23,\ 0.13,\ 0.11,\ 0.17,\ 0].$$

For both positions, the diffusive term is the dominant one, with a coefficient equal to *1.1*, indicating a Prandtl number near *0.9*. When one or two of the parameters, other than $t_i{}^*\text{-}\Gamma_N{}^*$ and R/L_n is left out, fits for $\varepsilon = 0.255$ are only marginally worse (e.g. $\sigma = 1.85$ instead of $\sigma = 1.74$), but the coefficients for the remaining variables are little changed. This suggests that the dependencies are fairly robustly obtained by this procedure. The influence of magnetic shear, $s = \varepsilon R/L_q$, as determined by the default version of EFIT[52] at JET (without internal constraints), was found to be insignificant and statistically irrelevant at $\varepsilon = 0.255$.

We caution, that due to uncertainties and correlations in the data, as well as due to the simplicity of linear regressions, the coefficients obtained may not truthfully reflect the underlying physics dependencies. Also, as only a single parameter is used for the diffusive part, any parameter dependencies of the Prandtl number (as theoretically expected) will 'spill over' into the remaining regression variables. For $\varepsilon = 0.165$, it is unlikely that only the single variable T_i/T_e determines the non-diffusive transport components. In all likelihood there are several, but the corresponding coefficients cannot be determined with sufficient significance because of experimental errors.

We now seek to provide a global fit that is satisfactory for all values of ε in the dataset, i.e. $0.075 \le \varepsilon \le 0.255$. Correlations between the variables are reinforced, because they now also correlate through their radial dependencies. However it also allows to include $f_t = \varepsilon^{1/2}$ as an important physics variable. Fortunately, the dependencies obtained from global fits largely reflect the local ones.

Although good 6-parameter fits with $STS > 1$ for all variables are obtained, one or two have $STR < 0.08$. The best 5-parameter regression satisfying our significance and relevance criteria is shown in fig.6a and corresponds to the scaling expression

$$R/L_\omega \; 1.2(t_i{}^*\text{-}\Gamma_N{}^*) + 0.41R/L_n + 12\varepsilon^{1/2} + 0.41q\text{-}1.9T_i/T_e\text{-}1.7 \tag{6}$$

$$\text{with } \sigma = 1.29,\ STS = [18,\ 5.8,\ 8.2,\ 3.5,\ 3.1,\ 1.9] \text{ and } STR = [0.52,\ 0.2,\ 0.28,\ 0.09,\ 0.08,\ 0];$$

The diffusive component remains the most significant and relevant one, with $STR = 0.52$, meaning

that overall about half of the variation of R/L_ω in the dataset can be attributed to diffusion, with the remainder to be attributed to non-diffusive processes. While there is a strong dependence on $\varepsilon^{1/2}$, corresponding to *STR = 0.28*, the coefficients for *R/Ln*, *q* and T_i/T_e remain similar to the ones in the local fits (eq. 4 & 5), suggesting that the global regression including $\varepsilon^{1/2}$ does not significantly bias the dependencies found in fits for fixed values of ε.

In order to provide a test for the influence of $\varepsilon^{1/2}$ on the regressions, we performed a 5-parameter regression not including this variable, shown in fig6.b):

$$R/L_\omega \; 1.1(t_i^*\text{-}\Gamma_N^*) + 0.66R/L_n + 0.29R/L_{Te} + 0.4q\text{-}3.5T_i/T_e + 2.5 \qquad (7)$$

with $\sigma = 1.38$, *STS = [15, 9.8, 4.9, 3.1,5.6, 3.3]* and *STR = [0.49, 0.32, 0.16, 0.09, 0.14, 0];*

The result is a reinforcement of the dependencies on R/L_n and T_i/T_e and R/L_{Te} towards the upper boundaries of their respective confidence intervals in eq.(5 and 6). This suggests that a variable directly sensitive to the radial dependence, such as $\varepsilon^{1/2}$, is indeed required for a good regression encompassing the whole range of ε in the dataset.

The above regressions raise the question as to the ultimately lowest achievable standard deviation using a small set of variables and without over-fitting. To answer this question we have executed a few dozen regressions using neural networks with a range of neuron numbers (9-50) in the hidden layer. Neural network regressions have the advantage of requiring no a priori assumptions on the functional forms of the target variable dependencies and the disadvantage of providing little interpretable insight. Half of the samples, selected at random, were used for training, one quarter for validating during the training iterations and the final quarter was used for final testing of the quality of the regressions. Using the variables $(t_i^*\text{-}\Gamma_N^*)$, R/L_n, R/L_{Te}, T_i/T_e, *q* and *s,* the best networks, assessed on the test set, achieved $\sigma \approx 1.15$. This is only slightly better than the best linear regressions using these six variables ($\sigma \approx 1.25$), showing that the simple linear regressions do capture the main dependencies and provide regressions close to the best possible. When all variables in table 1 were included, the best neural networks achieved $\sigma \approx 1$ on the test set, which we regard as the noise floor for these regressions.

Parameter dependencies of non-diffusive momentum transport were also obtained from NBI modulation experiments [3]. However, as this dataset was very small (12 samples), multiple dependencies could not be resolved. The main result obtained in ref.[3] was a scaling for the pinch number with R/L_n : $RV_\phi/\chi_\phi \approx 1.2R/L_n$. While this is clearly much stronger than obtained from the above multi-parameter scalings, $RV_\phi/\chi_\phi \approx 0.4R/L_n$+..., these findings are not inconsistent with ours when correlations are considered. A global two-parameter fit (not shown) assuming only on a diffusive term and a term proportional to R/L_n is obtained with $\sigma = 1.54$ as $R/L_\omega \approx 1.3(t_i^*\text{-}\Gamma_N^*) + 0.81R/L_n + 0.59$. It is hence likely that the R/L_n dependence in ref. [3] would decrease if more parameter dependencies could be introduced. This would require extending the modulation database and would unfortunately be quite challenging because of the large number of specific modulation experiments and the amount of labour involved in the analysis of modulation data.

One should not dismiss scaling relations derived from a correlated database such as the one available for this study as useless for predictions. The handful of alternative good scalings we obtain may well diverge outside the regression domain, but inside that domain, they are equivalent. ITER is expected to have a similar dimensionless operating domain as the larger contemporary tokamaks, with the notable exceptions of ρ_i^* and probably u. In none of the satisfactory regressions does ρ_i^* appear with any statistical significance or statistical relevance, suggesting that the dependencies of the Coriolis pinch may be similar to those seen in JET. However, because of the lower Mach number in ITER, the balance between the Coriolis pinch and residual stresses is likely to be different in ITER, which will have a weaker external momentum input, in normalised terms, than JET.

7. COMPARISON WITH LINEAR GYROKINETIC MODELLING

To compare the parametric dependencies obtained in the experiments to the theoretical predictions, a representative subset of 420 samples of the database was used as input for a series of linear gyrokinetic calculations performed with the δf flux-tube code GKW [57]. This subset was selected such as to remain representative of the same dimensionless parameter domain as the entire experimental dataset. The calculations were performed for two representative wave vectors, $k_\theta\rho_i = 0.15$ & 0.45, where $k_\theta\rho_i = 0.45$ roughly corresponds to the wave vector of maximum growth rate, assuming a circular geometry, electrostatic fluctuations and two kinetic species (deuterons and electrons). In the present database with $O_{rs} = \rho_i^*(R/L_{Ti})^2/u < 1$ for most cases, the pinch is expected to be the largest non-diffusive contribution to the momentum flux [21] and the simulations were therefore performed without background E×B shear flow or other residual stress contributions. The dominant instability was identified to be the Ion Temperature Gradient (ITG) mode. For each input parameter combination, two calculations were performed. The first of these, with $u = 0.1$ and $u' = uR/L_\omega = 0$ provided the momentum pinch part, while the second, with $u = 0$ and $u' = 1$ provided the diagonal (diffusive) part. The Prandtl and pinch numbers were then deduced from the fluxes obtained in each case as described in ref.[58]. The resulting change in momentum flux (i.e. torque t) allows a separation into a diffusive and a pinch contribution, the former being characterised by $R/L_\omega \mu t$. Collisional and non-collisional calculations mostly produce similar results, in agreement with refs [27, 35]. A few additional simulations were performed with the full MHD equilibrium, confirming that the up-down asymmetry residual stress [59] is negligible in the core of these plasmas and that the circular flux surfaces assumption provides, within 15%, similar Prandtl and pinch numbers, and barely affects their parametric dependencies. The choice of linear simulations for this statistical comparison is mainly dictated by practical reasons, however, it is also supported by the fact that the dominant parametric dependencies of the pinch number are largely similar in linear [23] and non-linear calculations [21]. In fig.7, we see that the predicted pinch number and Prandtl numbers at $k_\theta\rho_i = 0.15$ & 0.45 are of the required magnitude and, more importantly, that the radial dependence of the pinch number is well reproduced. A more detailed comparison would require a suitable spectral average over the entire unstable domain (typically $0.05 < k_\theta\rho_i < 1.5$), as

introduced for instance in the TGLF quasi-linear momentum transport model [60] or even much more laborious non-linear calculations. The linear calculation at $k_\theta\rho_i = 0.15$ and 0.45 however provide a rather good proxy of the non-linear results. The spectral averages for linear calculations are expected to fall between the ones for those two wavenumbers. A sample-by-sample comparison, using for simplicity the average Prandtl and pinch numbers from the GKW calculations, shows a fair agreement of theoretically expected and observed R/L_ω, although predicted values fall typically 30% short of the experimental ones, as seen in fig.8.

The data in fig.8 are resolved into classes of the ordering parameter $O_{rs} = \rho_i*(R/L_{Ti})^2/u$. As expected, agreement between experiment and the modelling with only the Coriolis pinch is best for the lowest values of this parameter. The predictions for samples with smallest O_{rs}, e.g. $O_{rs}<0.25$ (stars) are on average 86% of the experimental values, while than those with the largest O_{rs}, e.g. $O_{rs}>1$ (diamonds) are on average 65% of the observed values. The parametric trends in the modelled data can be inferred by regressions, much in the same way as experimental data, with however, the advantage that, unlike for the experimental data, there is no need for separating the diffusive and non-diffusive components. The theoretically predicted data, with input parameters taken from the experimental database, are subject to the same correlation issues as the experimental data. This is an advantage for comparisons because correlation-induced biases are similar. However it should be kept in mind, before we proceed with presenting the results, that such linear fits, however popular, ultimately fail to capture the complex and non-linear dependencies of the transport coefficients on the input parameters (see fig.2 in ref.[23]).

In figure 9 we show the best multi-parameter fits for the average pinch number for $k_\theta\rho_i = 0.15$ and 0.45, satisfying our significance criteria for the same positions as the experimental data in fig.5.

These regressions correspond to

$$\text{at } \varepsilon = 0.165\text{: } RV/\chi_\phi \approx 0.35R/L_n + 0.052R/L_{Te} + 0.17T_i/T_e + 0.59q + 0.36s - 1.2 \quad (8)$$
$$\text{with } \sigma = 0.2,\ STS = [4.5,\ 1,\ 0.5,\ 5,\ 1.9,\ 2.2] \text{ and } STR = [0.53,\ 0.13,\ 0.06,\ 0.69,\ 0.25,\ 0];$$

$$\text{at } \varepsilon = 0.255\text{: } RV/\chi_\phi \approx 0.45R/L_n + 0.052R/L_{Te} + 0.88T_i/T_e + 0.29q - 0.24s - 0.23 \quad (9)$$
$$\text{with } \sigma = 0.32,\ STS = [11,\ 2,\ 2.8,\ 3.8,\ 3.3,\ 0] \text{ and } STR = [0.88,\ 0.17,\ 0.22,\ 0.27,\ 0.26,\ 0].$$

The coefficients for the two most relevant parameters, R/L_n (STR = 0.53 and 0.88) and q ($STR = 0.69$ and 0.27) are very close to those obtained from the experiment for $\varepsilon = 0.255$. Note that for comparison with the experiment, the STR should be normalised to the non-diffusive part (1-STR) in the experiment. Unlike in the experimental dataset, the magnetic shear is seen as significant, but position dependent. In the experimental dataset q and s are provided by EFIT calculations only based on external magnetic measurements and are therefore not reliable. As this version of EFIT provides little freedom, a meaningful comparison of the theoretical and experimental magnetic shear dependences is not possible using the presently available dataset. For $\varepsilon = 0.255$, the theoretical

data show a T_i/T_e dependence, which is opposite to that obtained from the experimental data.

The best global 5 parameter regression, shown in fig.10 for the average theoretical pinch is obtained, with $\sigma = 0.35$ as:

$$RV/\chi_\phi \approx 0.44R/L_n + 0.077R/L_{Te} + 0.31q - 0.21s + 6.8\varepsilon^{1/2} - 2.8 \qquad (10)$$

with $s = 0.31$, $STS = [17, 4.7, 7, 4.6, 6.4, 7.3]$ and $STR = [0.73, 0.16, 0.22, 0.27, 0.33, 0]$.

The coefficients are similar to those obtained for the two local fits (eq. 8 & 9), with the exception of s, which, as mentioned cannot be compared with the experiment because of the limitations of the standard version of EFIT in JET. The coefficients for R/L_n, q and $\varepsilon^{1/2}$ are also close to those from the experiment, although the theory-derived coefficient for $\varepsilon^{1/2}$ is clearly lower than the experimental one. The coefficient for R/L_{Te} is also consistent in magnitude and sign with the experimental values obtained in most experimental multi-parameter fits, although the experimental STS and STR for R/L_{Te} are often marginal. These similarities in the parameter dependencies further support the identification of the observed non-diffusive transport with the theoretically predicted Coriolis pinch.

8. POSSIBLE RESIDUAL STRESS CONTRIBUTIONS

The difference between observed rotation frequency gradients and those predicted assuming that the Coriolis pinch is the only non-diffusive transport mechanism is an indication that residual stresses may contribute to the inward momentum transport in at least part of the plasmas investigated. The differences in scaling with T_i/T_e also suggest that the Coriolis pinch may not be the only non-diffusive mechanism. Referring to fig.8, samples with $O_{rs}>1$ have normalised rotation frequency gradients which are on average some 25% larger than those with $O_{rs}<0.25$, suggesting that for $O_{rs}>1$, the residual stresses may contribute approximately 25% or more to R/L_ω. Since the diffusive contribution is typically 50%, this means that for the samples with $O_{rs}>1$ (8% of the samples in the database), the Coriolis pinch and residual stresses may be roughly equally important, but also imply that for $O_{rs}<0.25$, the contribution of residual stresses to R/L_ω may only be in the percent range.

We have attempted regressions of the form of eq. (2) including terms of the form $1/u$ and $R/(uL_n)$., The latter was suggested by the recent observation in the core of AUG plasmas of a strong correlation between the value of R/L_ω at zero rotation and the logarithmic density gradient R/L_n [61]. The coefficient obtained for $R/(uL_n)$ is robustly around 0.07 for global regressions and around 0.1 for $\varepsilon > 0.15$, independently of the other parameters in the regression. For the average $R/(L_\omega) \sim 14$ in the database, this represents a typical contribution of around 1 to the non-diffusive component of R/L_ω and up to about 2 for $\varepsilon > 0.15$, where $R/(uL_n)$ is larger. These numbers represent typically one third of the non-diffusive momentum flux.

The above estimates should not be taken as proof that residual stress contributions have definitely been identified in this database, since correlations in the database and the absence of theoretically documented dependencies for residual stresses still preclude a reliable discrimination between the

two transport mechanisms. However, they do show that the data leave the door open for a non-negligible residual stress contribution, which could account for part of the difference between the observed non-diffusive transport and the modeled Coriolis pinch. A detailed assessment of residual stresses will have to await the completion of systematic modeling studies akin to the ones presented here for the Coriolis pinch.

9. SUMMARY AND CONCLUSIONS

The analysis presented here shows that non-diffusive contributions to the momentum transport are ubiquitous in JET H-modes and hybrid scenarios and account overall for nearly half of the toroidal angular momentum transport. Their typical contribution to the normalized angular frequency gradient R/L_ω rises from near 1 in the core at $\varepsilon \sim 0.07$ to around 5 near the edge at $\varepsilon \sim 0.255$. This observed non-diffusive momentum transport is in good agreement with the theoretically expected Coriolis pinch, modeled using linear GKW calculations. Multi-parameter regressions were performed both on nearly 1000 experimental samples and over 300 samples obtained from the GKW calculations. The experimental regressions indicate a Prandtl number near 0.9, which is consistent with the values from GKW, which rise from around 0.6 at $\varepsilon = 0.075$ to around 1 for $\varepsilon = 0.255$. The non-diffusive components from the best regressions including the largest number of statistically significant and relevant parameters correspond to

$$RV/\chi_\phi + \tau_{rs}*/u \; 0.41R/L_n + 0.41q + 12\varepsilon^{1/2} - 1.9T_i/T_e - 1.7 \quad (11)$$

from eq.(6) for the experiment and

$$RV/\chi_\phi \approx 0.44R/L_n + 0.31q + 6.8\varepsilon^{1/2} + 0.077R/L_{Te} - 0.21s - 2.8 \quad (10)$$

from GKW for the Coriolis pinch.

The two regressions have similar dependencies for the parameters with the highest relevance, R/L_n, $\varepsilon^{1/2}$ and q, supporting the prediction, that the Coriolis pinch is the main non-diffusive momentum transport mechanism in rotating NBI-heated JET H-modes and hybrid scenarios. The experimental values for $RV/\chi_\phi + \tau_{rs}*/u$ are however about 50% higher than those for RV/χ_ϕ expected from the Coriolis pinch alone. Further studies are required in order to assess to which extent this difference may be explained by residual stresses. Importantly, no significant or relevant dependencies on ρ_i* and β were found in the experimental data, nor are such dependencies theoretically expected for the Coriolis pinch. The absence of a dependence on ρ_i* suggests that our empirical and theoretical scalings for the Coriolis pinch may be extrapolated to ITER discharges with the same dimensionless parameters other than ρ_i*. Although the Coriolis pinch must be expected to play a role in any rotating plasma, the rotation profile in ITER is likely to differ significantly from the one observed in JET because the balance of the torques, the pinch and the residual stresses in ITER will be very different from JET.

ACKNOWLEDGMENTS / DISCLAIMERS

The authors wish to acknowledge stimulating discussions wihth C. Angioni and helpful suggestions

and criticism by the referees. The calculations for this work were performed using HPC resources from GENCI-CCRT/IDRIS (Grant 2012 - 100182). This work was supported by EURATOM and carried out within the framework of the European Fusion Development Agreement. The views and opinions expressed herein do not necessarily reflect those of the European Commission.

REFERENCES

[1]. J.E. Rice, Nuclear Fusion **47**, 1618 (2007)
[2]. T. Tala et al, Physical Review Letters **102**, 075001 (2009)
[3]. T. Tala et al, Nuclear Fusion 123002 **51** (2011)
[4]. A. Bortolon et al, Physical Review Letters **97**, 235003 (2006)
[5]. R.M. McDermott, Plasma Physics and Controlled Fusion **53**, 035007 (2011)
[6]. J.E Rice et al, Nuclear Fusion **51** (2011) 083005
[7]. S.H. Müller et al, Physical Review Letters **106**, 115001 (2011)
[8]. W.M. Solomon et al, Nuclear Fusion **51** (2011) 073010
[9]. K. Nagashima et al., Nuclear Fusion **34** (1994) 449
[10]. K. Ida et al., Physical Review Letters **74** (1995) 1990
[11]. W.D. Lee et al., Physical Review Letters **91** (2003) 205003
[12]. J.E. Rice et al., Nuclear Fusion **44** (2004) 379
[13]. M. Yoshida et al., Physical Review Letters **103** (2009) 065003
[14]. K. Ida et al., Nuclear Fusion **52** (2010) 064007
[15]. M.Yoshida et al. Nuclear Fusion **53** (2012) 023024
[16]. L.G. Eriksson L-G et al, Plasma Physics and Controlled Fusion **39** (1997) 27
[17]. J.E. Rice et al, Nuclear Fusion **38** (1998) 75
[18]. I.H. Hutchinson et al, Physical Review Letters **84** (2000) 3330
[19]. G.T. Hoang et al Nuclear Fusion **40** (2000) 913
[20]. J.S. deGrassie et al, Physics of Plasmas **11** (2004) 4323
[21]. A.G. Peeters et al, Nuclear Fusion, **51**, 094027 (2011)
[22]. C. Angioni, submitted Nuclear Fusion, this volume (invited)
[23]. A.G. Peeters et al, Physical Review Letters **98** 265003 (2007)
[24]. T.S. Hahm et al, Physics of Plasmas **14**, 072302 (2007)
[25]. R.E. Waltz et al, Physics of Plasmas **14**, 122507 (2007)
[26]. A.G. Peeters et al, Physics of Plasmas **16**, 042310 (2009)
[27]. A.G. Peeters et al, Physics of Plasmas **16**, 062311 (2009)
[28]. J. Weiland et al, Nuclear Fusion **49**, 065033 (2009)
[29]. A.I. Smolyakov et al, Nuclear Fusion **49**, 125001 (2009)
[30]. P.H. Diamond et al., Physics of Plasmas **15**, (2008) 012303
[31]. P.H. Diamond et al, Nuclear Fusion **49** 045002 (2009)
[32]. O.D. Gurcan et al., Physical Review Letters **100**, (2008) 135001

[33]. T.S. Hahm et al., Physics of Plasmas **15**, (2008) 055902
[34]. E.S. Yoon et al., Nuclear Fusion **50**, (2010) 064006
[35]. N. Kluy et al, Physics of Plasmas **16**, 122302 (2009)
[36]. T. Hein et al, Physics of Plasmas **18**, 072503 (2011)
[37]. F. Romanelli and R. Kamendje, Nuclear Fusion **49**, 104006 (2009)
[38]. Joffrin E. et al. in Fusion Energy 2010 (Proc. 23rd Int. Conf. Daejeon, 2010) (Vienna: IAEA) CD-ROM file EX/1-1 and http://www-naweb.iaea.org/napc/physics/FEC/FEC2010/html/index.htm
[39]. M Shimada et al. Progress in the ITER Physics Basis Chapter 1: Overview and summary 2007 Nuclear Fusion **47** S1
[40]. A. Zabolotsky et al, Nuclear Fusion **46**, (2006) 594
[41]. P.C. de Vries et al, Nuclear Fusion **48**, 035007 (2008)
[42]. H. Weisen et al, Plasma Physics and Controlled Fusion **48** (2006) A457–A466
[43]. M. Maslov et al 2009 Nuclear Fusion **49** 075037
[44]. P.C. de Vries, M.D. Hua et al, Nuclear Fusion **48**, 065006 (2008)
[45]. C. Giroud et al, Review of Scientific Instruments **79** (2008) 10F525
[46]. R. Pasqualotto et al, Review of Scientific Instruments **75**, 3891 (2004)
[47]. C.W. Gowers et al, Review of Scientific Instruments **66** (1995) 471
[48]. E.J. Doyle et al. Progress in the ITER Physics Basis Chapter 2: Plasma confinement and transport 2007 Nuclear Fusion **47** S18
[49]. P. Mantica et al, Physical Review Letters **107** (2011) 135004
[50]. C.D. Challis et al, Nuclear Fusion **29** (1989) 563
[51]. J.A. Heikkinen *et al*., Journal of Computational Physics **173** (2001) 527
[52]. L.L. Lao et al., Nuclear Fusion **25** (1985) 1421
[53]. M. J. Mantsinen, C. Angioni, L.-G. Eriksson et al, Plasma Physics and Controlled Fusion **44** (2002) 1521
[54]. M.F.F. Nave et al, "JET intrinsic rotation studies in plasmas with a high normalised beta and varying toroidal field ripple", to be published in Plasma Physics and Controlled Fusion, special issue "JET Task Force H 2011", March 2012
[55]. J.-M. Noterdaeme et al, Nuclear Fusion **43**, 274 (2003)
[56]. T.W. Versloot, Ph.D thesis, Eindhoven University of Technology, The Netherlands (2011), http://repository.tue.nl/715588
[57]. A. G. Peeters et al., Computer Physics Communications, **180** (2009) 2650
[58]. Y. Camenen et al., Nuclear Fusion **51**, 073039 (2011)
[59]. Y. Camenen et al, Physical Review Letters **102**, (2009) 125001
[60]. G.M. Staebler et al., Physics of Plasmas **18**, 056106 (2011)
[61]. C. Angioni et al, Physical Review Letters **107** (2011) 215003

	$\lvert t_i^*-\Gamma_N^*\rvert$	u	R/L_ω	R/L_n	R/L_{Ti}	R/L_{Te}	T_i/T_e	ε	ν_{eff}	β	ρ_i^*	q	s
min	0.05	0.05	0.4	1	3	3	0.6	0.075	0.06	0.001	0.001	0.9	0.01
max	14	0.38	24	10	19	17	2.7	0.255	5.2	0.049	0.005	4.6	10

Table 1: Dimensionless parameter ranges in JETPEAK H-mode and hybrid database. Here $u = R\omega/v_i = R\omega/(2T_i/m_i)^{1/2}$ *is the Mach number,* $L_\omega = \omega/\nabla\omega$ *etc,* $\varepsilon = r/R$ *is the inverse aspect ratio,* $n_{eff} = 10^{-14} R Z_{eff} n_e T_e^{-2}$ *is the normalised collisionality,* β *is the local thermal plasma pressure normalised to the magnetic pressure,* $\rho_i^* = (2T_i/m_i)^{1/2}/(\omega_{ci}R)$ *is the thermal ion Larmor radius normalised to R, q is the local safety factor obtained using the equilibrium code EFIT [52] and* $s = \varepsilon R/L_q$.

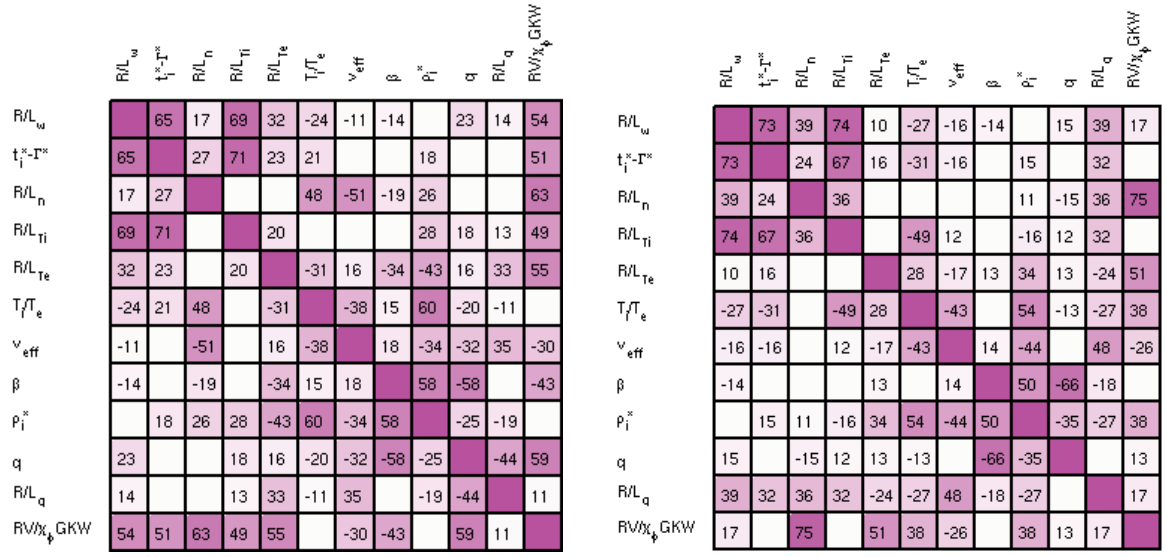

Table 2: Normalised covariances in % between dimensionless quantities. Values below 10% are below the significance level and are blanked. Table 2a), left: $\varepsilon = 0.165$, *Table 2b), right* $\varepsilon = 0.255$. *The last line refers to the theoretically predicted Coriolis pinch, presented in section 7. For these the significance level is about 25% due to the small sample size.*

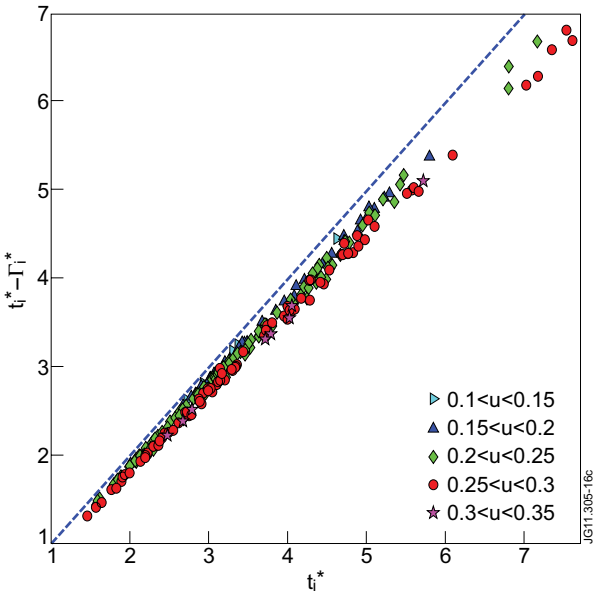

Figure 1: Net dimensionless torque corrected for particle flux versus gross dimensionless torque at mid-radius. Symbols refer to classes of Mach numbers.

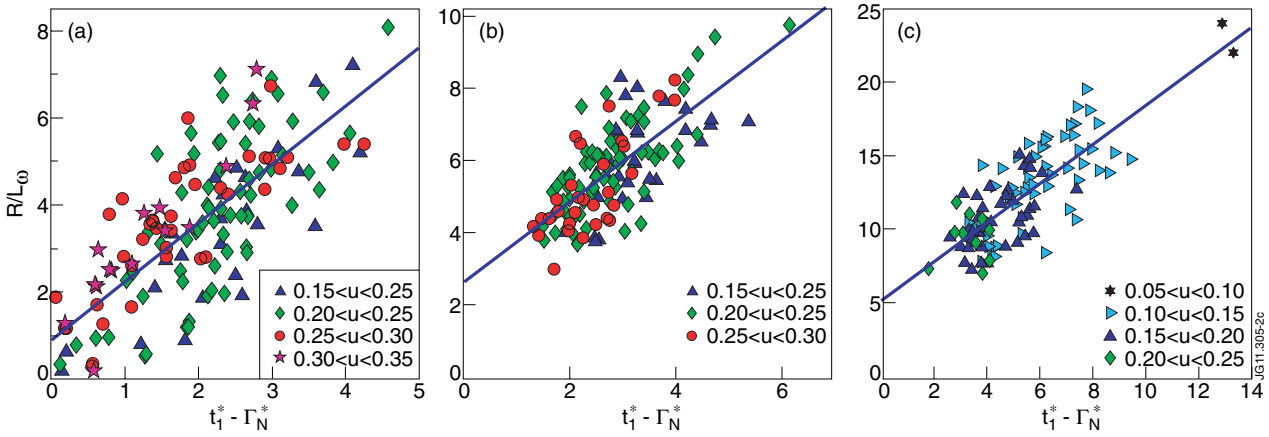

Figure 2: Fits of eq.(2), showing a diffusive component (slope) and a non-diffusive component (intercept at zero effective torque) for three positions, a) $\varepsilon \approx 0.075$ ($r/a \approx 0.25$) b) $\varepsilon \approx 0.165$ ($r/a \approx 0.55$) and c) $\varepsilon \approx 0.255$ ($r/a \approx 0.85$). The symbols refer to classes of Mach number u.

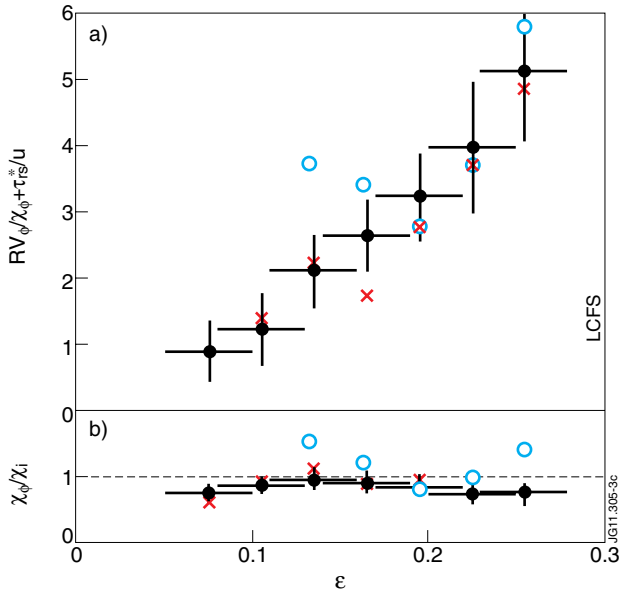

Figure 3: Average convection number (a) and Prandtl number (b) for seven radial intervals. The black symbols refer to our main dataset, the blue circles to a dataset used to study the momentum pinch using NBI modulation, the x signs to a set of discharges with TF ripple varied in the range 0.08-1%.

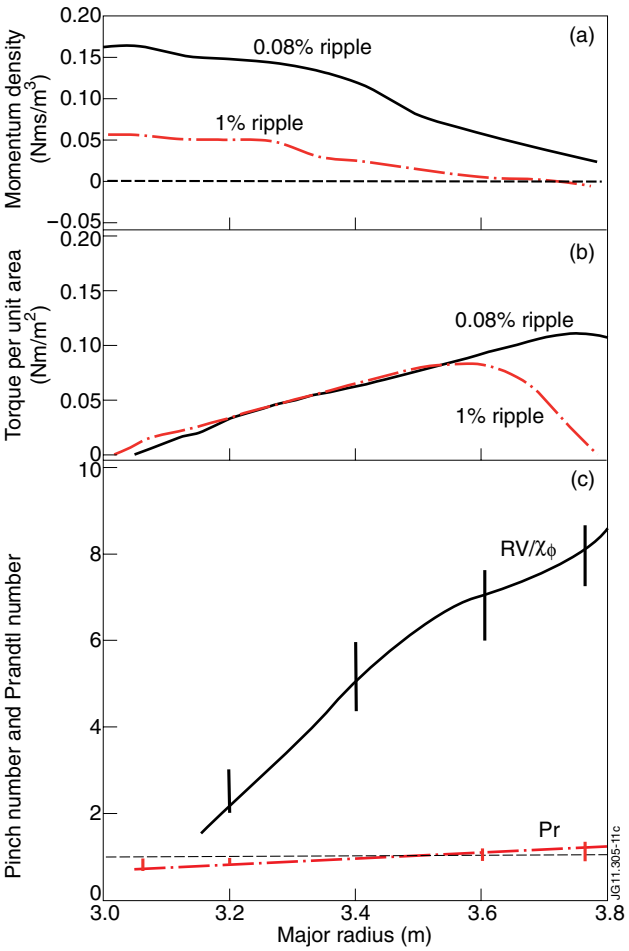

Figure 4: Comparison of H-modes with low and high toroidal ripple.
a) Momentum density profile for a 0.08% ripple case (solid black line) and a 1% ripple case (dash-dotted red line).
b) Corresponding torque profiles calculated using ASCOT.
c) Pinch number and Prandtl number profile and ranges (bars) allowing a good simulation of both cases.

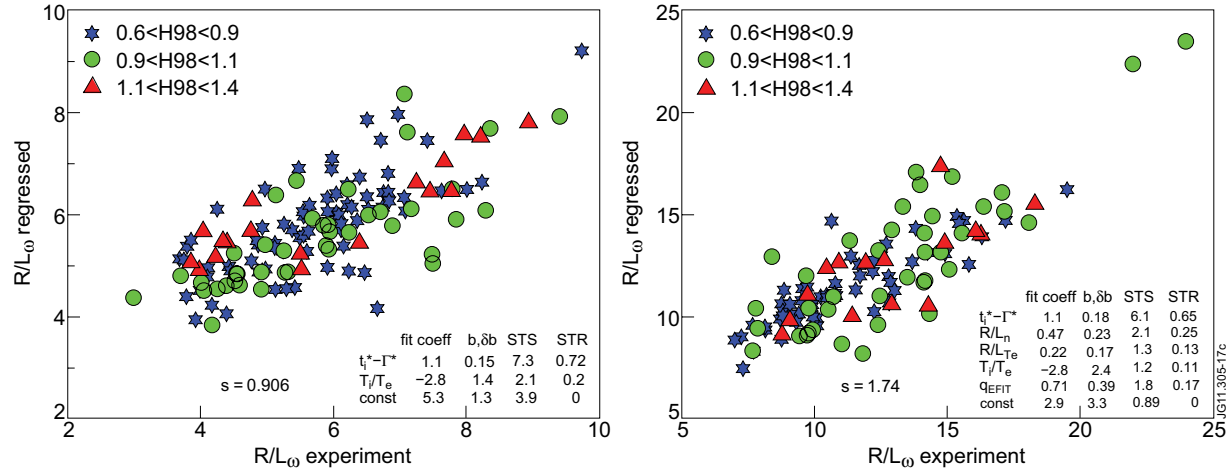

Figure 5: Best multi-parameter regressions for ε = 0.165 (mid-radius) and 0.255 (near the edge). The symbols refer to the H98 confinement factor. The embedded table shows the regression variables, the coefficients (b) and their 90% confidence half interval δb, the statistical significance (STS) and relevance (STR).

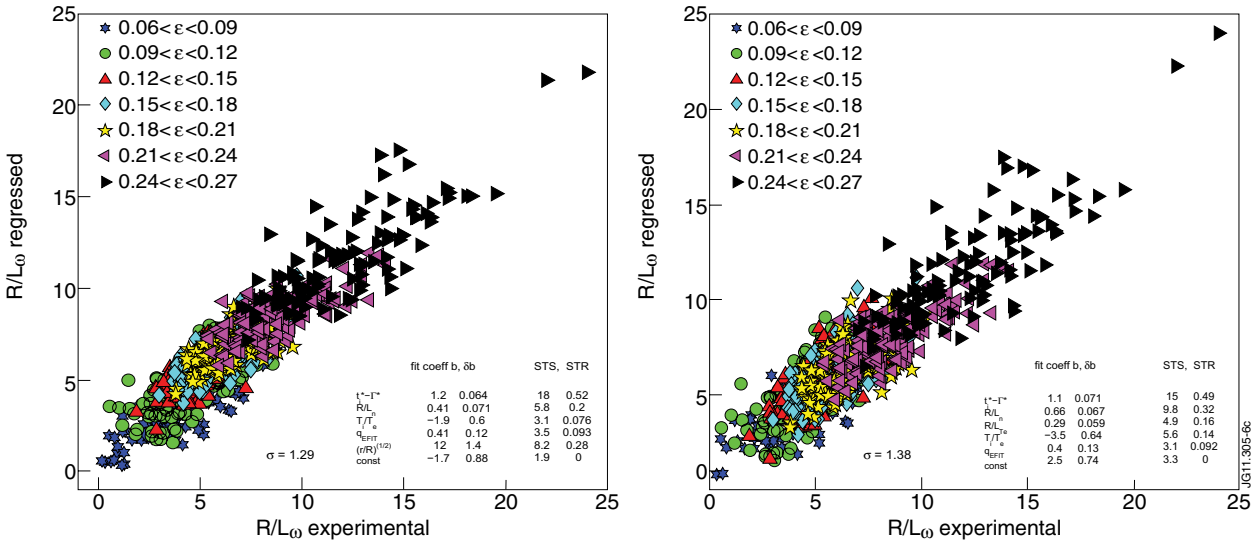

Figure 6: a) Left: Best global 5-parameter regressions for R/L_ω. b) Right: Best 5 parameter regression not including $\varepsilon^{1/2}$ as a regression variable. The symbols refer to the local inverse aspect ratio ε = r/R.

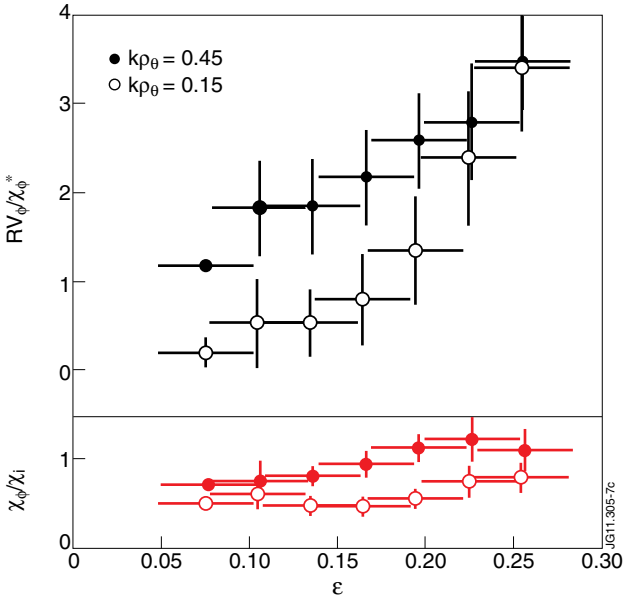

Figure 7: Average and standard deviation (bars) of Prandtl (red) and pinch numbers (black) from GKW, for two different wavenumbers.

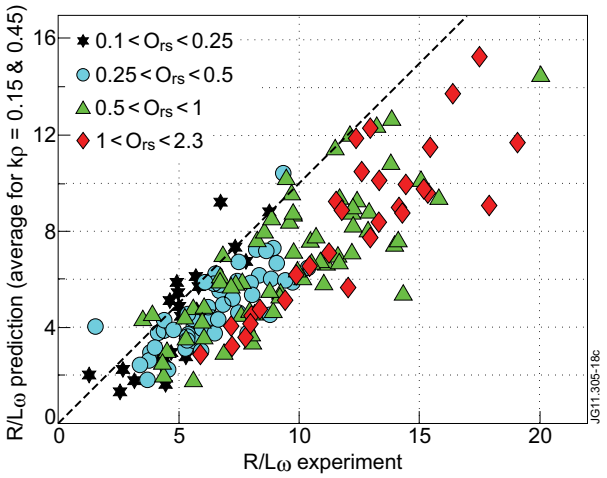

Figure 8: Sample-by-sample comparison of experimental and modeled R/L_ω. The symbols refer to the ordering parameter $O_{rs} = \rho_i^*(R/L_{Ti})^2/u$.

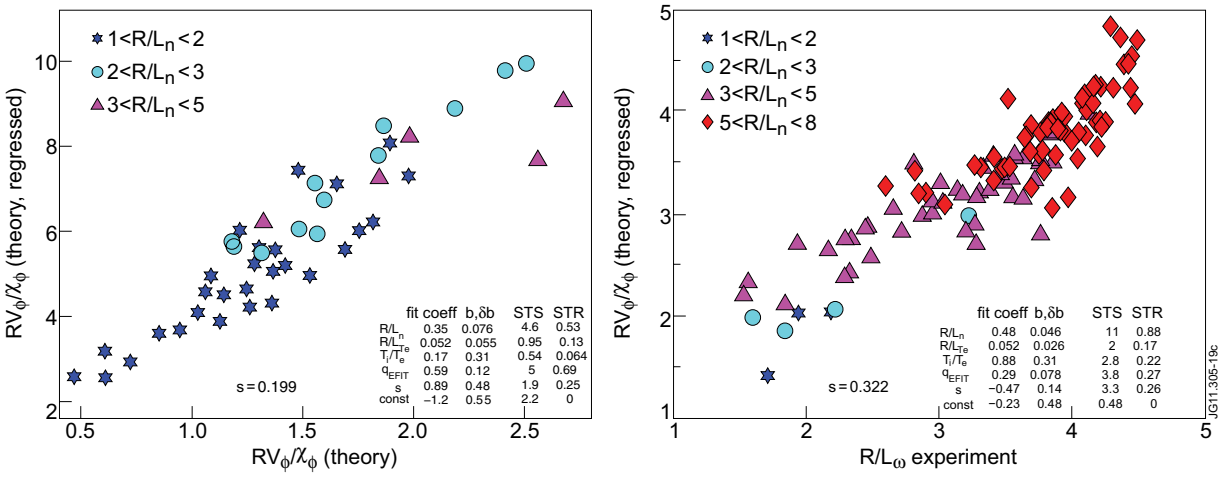

Figure 9: Regressions for the theoretical Coriolis pinch number. a) Left: ε =0.165 (mid-radius) and b) Right: ε =0.255 (near the edge). The symbols refer to the normalized density gradient R/L_n.

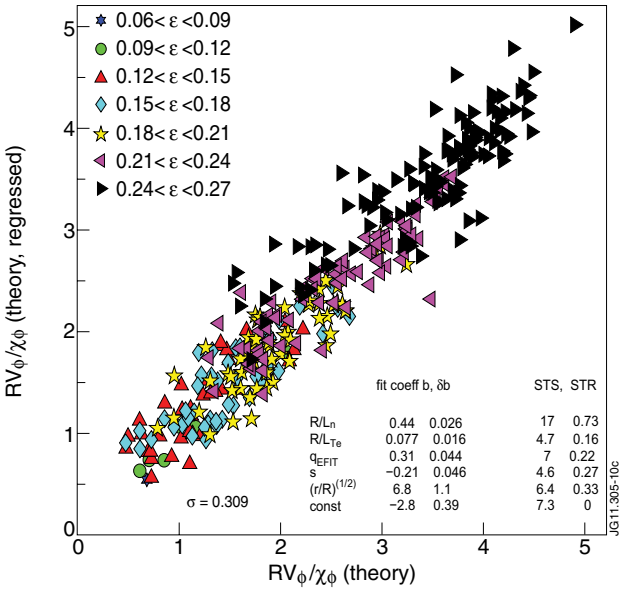

Figure 10: Best global 5-parameter regressions for the theoretical Coriolis pinch number. For comparison with the experimental regression (fig. 6), which also contains the diffusive part, the STR in this regression should be divided by 2.